An ultra-potent synthetic nanobody neutralizes SARS-CoV-2 by locking Spike into an inactive conformation — Source link ⧉

Michael Schoof, Bryan Faust, R.A. Saunders, Smriti Sangwan ...+57 more authors

Institutions: University of California, San Francisco, Pasteur Institute, University of California, Berkeley, Gladstone Institutes ...+2 more institutions

Related papers:

- An ultra-high affinity synthetic nanobody blocks SARS-CoV-2 infection by locking Spike into an inactive conformation

- Neutralizing nanobodies bind SARS-CoV-2 spike RBD and block interaction with ACE2.

- Cryo-EM structure of the 2019-nCoV spike in the prefusion conformation.

- Structural Basis for Potent Neutralization of Betacoronaviruses by Single-Domain Camelid Antibodies.

- Structure, Function, and Antigenicity of the SARS-CoV-2 Spike Glycoprotein.

1 **TITLE:** An ultra-potent synthetic nanobody neutralizes SARS-CoV-2 by locking Spike into an
2 inactive conformation
3
4 Michael Schoof[1,2#*], Bryan Faust[1,2,3,4#], Reuben A. Saunders[1,5#], Smriti Sangwan[1,2#], Veronica
5 Rezelj[6#], Nick Hoppe[3,4], Morgane Boone[1,2], Christian B. Billesbølle[3,4], Cristina Puchades[4],
6 Caleigh M. Azumaya[4], Huong T. Kratochvil[4], Marcell Zimanyi[1,2], Ishan Deshpande[3,4], Jiahao
7 Liang[3], Sasha Dickinson[4], Henry C. Nguyen[4], Cynthia M. Chio[4], Gregory E. Merz[4], Michael C.
8 Thompson[4], Devan Diwanji[4], Kaitlin Schaefer[4], Aditya A. Anand[1,2], Niv Dobzinski[1,2], Beth
9 Shoshana Zha[7], Camille R. Simoneau[10,11,12], Kristoffer Leon[10,11,12], Kris M. White[13,14], Un Seng
10 Chio[4], Meghna Gupta[4], Mingliang Jin[4], Fei Li[4], Yanxin Liu[4], Kaihua Zhang[4], David Bulkley[4], Ming
11 Sun[4], Amber M. Smith[4], Alexandrea N. Rizo[4], Frank Moss[4], Axel F. Brilot[4], Sergei Pourmal[4],
12 Raphael Trenker[4], Thomas Pospiech[4], Sayan Gupta[9], Benjamin Barsi-Rhyne[3], Vladislav
13 Belyy[1,2], Andrew W. Barile-Hill[8], Silke Nock[1,2], Yuwei Liu[1,2], Nevan J. Krogan[4,5,10,11], Corie Y.
14 Ralston[9], Danielle L. Swaney[4,5,10,11], Adolfo García-Sastre[13,14,15,16], Melanie Ott[10,11,12], Marco
15 Vignuzzi[6], QCRG Structural Biology Consortium[4‡], Peter Walter[1,2*], Aashish Manglik[3,4,10,17*]
16
17 **AFFILIATIONS:**
18 [1]Howard Hughes Medical Institute, University of California at San Francisco, San Francisco, CA,
19 USA.
20 [2]Department of Biochemistry and Biophysics, University of California at San Francisco, San
21 Francisco, CA, USA.
22 [3]Department of Pharmaceutical Chemistry, University of California at San Francisco, San
23 Francisco, CA, USA.
24 [4]Quantitative Biosciences Institute (QBI) Coronavirus Research Group Structural Biology
25 Consortium, University of California, San Francisco, CA, USA.
26 [5]Department of Cellular and Molecular Pharmacology, University of California at San Francisco,
27 San Francisco, CA, USA.
28 [6]Viral Populations and Pathogenesis Unit, CNRS UMR 3569, Institut Pasteur, 75724, Paris,
29 Cedex 15, France
30 [7]Department of Pulmonary, Critical Care, Allergy and Sleep Medicine, University of California
31 San Francisco, San Francisco, CA 94158, USA.
32 [8]Cytiva Life Sciences, Marlborough, MA, USA.
33 [9]Molecular Biophysics and Integrated Bioimaging and the Molecular Foundry, Lawrence
34 Berkeley National Laboratory, Berkeley, CA, USA.
35 [10]Quantitative Biosciences Institute (QBI), University of California San Francisco, San
36 Francisco, CA, USA.
37 [11]J. David Gladstone Institutes, San Francisco, CA, USA.
38 [12]Department of Medicine, University of California San Francisco, San Francisco, CA, USA.
39 [13]Department of Microbiology, Icahn School of Medicine at Mount Sinai, New York, NY, USA.
40 [14]Global Health and Emerging Pathogens Institute, Icahn School of Medicine at Mount Sinai,
41 New York, NY, USA.
42 [15]Department of Medicine, Division of Infectious Diseases, Icahn School of Medicine at Mount
43 Sinai, New York, NY, USA
44 [16]The Tisch Cancer Institute, Icahn School of Medicine at Mount Sinai, New York, NY, USA
45 [17]Department of Anesthesia and Perioperative Care, University of California at San Francisco,
46 San Francisco, CA, USA.
47
48 # These authors contributed equally
49 ‡ Full listing in Supplementary Information
50 * To whom correspondence should be addressed; Email: michael@walterlab.ucsf.edu,
51 peter@walterlab.ucsf.edu, Aashish.Manglik@ucsf.edu

52 **ABSTRACT**

53 Without an effective prophylactic solution, infections from SARS-CoV-2 continue to rise

54 worldwide with devastating health and economic costs. SARS-CoV-2 gains entry into host cells

55 via an interaction between its Spike protein and the host cell receptor angiotensin converting

56 enzyme 2 (ACE2). Disruption of this interaction confers potent neutralization of viral entry,

57 providing an avenue for vaccine design and for therapeutic antibodies. Here, we develop single-

58 domain antibodies (nanobodies) that potently disrupt the interaction between the SARS-CoV-2

59 Spike and ACE2. By screening a yeast surface-displayed library of synthetic nanobody

60 sequences, we identified a panel of nanobodies that bind to multiple epitopes on Spike and

61 block ACE2 interaction via two distinct mechanisms. Cryogenic electron microscopy (cryo-EM)

62 revealed that one exceptionally stable nanobody, Nb6, binds Spike in a fully inactive

63 conformation with its receptor binding domains (RBDs) locked into their inaccessible down-

64 state, incapable of binding ACE2. Affinity maturation and structure-guided design of

65 multivalency yielded a trivalent nanobody, mNb6-tri, with femtomolar affinity for SARS-CoV-2

66 Spike and picomolar neutralization of SARS-CoV-2 infection. mNb6-tri retains stability and

67 function after aerosolization, lyophilization, and heat treatment. These properties may enable

68 aerosol-mediated delivery of this potent neutralizer directly to the airway epithelia, promising to

69 yield a widely deployable, patient-friendly prophylactic and/or early infection therapeutic agent to

70 stem the worst pandemic in a century.

71

72 **MAIN TEXT:**

73 Over the last two decades, three zoonotic β-coronaviruses have entered the human population,

74 causing severe respiratory symptoms with high mortality (*1-3*). The ongoing COVID-19

75 pandemic is caused by SARS-CoV-2, the most readily transmissible of these three

76 coronaviruses (*4-7*). SARS-CoV-2 has wrecked the world's economy and societies to an

77 unprecedented extent, to date (Aug. 14, 2020) causing 751,154

78 reported deaths around the globe (*8*). Although public health measures have slowed its spread

79 in many regions, infection hotspots keep reemerging. No successful vaccine or preventive

80 treatment has yet been manufactured for any coronavirus, and the time to develop an effective

81 and broadly available vaccine for SARS-CoV-2 remains uncertain. The development of novel

82 therapeutic and prophylactic approaches thus remains essential, both as temporary stopgaps

83 until an effective vaccine is generated and as permanent solutions for those segments of the

84 population for which vaccination proves ineffective or contraindicated.

85

86 Coronavirus virions are bounded by a membrane envelope that contains ~25 copies of the

87 homotrimeric transmembrane spike glycoprotein (Spike) responsible for virus entry into the host

88 cell (*9*). The surface-exposed portion of Spike is composed of two domains, S_1 and S_2 (*10*). The

89 S_1 domain mediates the interaction between virus and its host cell receptor, the angiotensin

90 converting enzyme 2 (ACE2), while the S_2 domain catalyzes fusion of the viral and host cell

91 membranes (*3, 11-13*). During its biogenesis, the Spike protein is proteolytically cleaved

92 between the S_1 and S_2 domains, which primes the virus for cellular entry (*10*). Contained within

93 S_1 is the receptor binding domain (RBD), which directly binds to ACE2. The RBD is attached to

94 the body of Spike by a flexible region and can exist in an inaccessible down-state or an

95 accessible up-state (*14, 15*). Binding to ACE2 requires the RBD in the up-state and enables

96 cleavage by host proteases TMPRSS2 or cathepsin, triggering a dramatic conformational

97 change in S_2 that enables viral entry (*16*). In SARS-CoV-2 virions, Spike oscillates between an

98 active, open conformation with at least one RBD in the up-state and an inactive, closed

99 conformation with all RBDs in the down-state (*9, 11, 14, 15*).

100

101 By screening a high-complexity yeast surface-displayed library of synthetic nanobodies, we

102 have uncovered a collection of nanobodies that block the Spike-ACE2 interaction. Biochemical

103 and structural studies revealed that two classes of these nanobodies act in distinct ways to

104 prevent ACE2 binding. Combining affinity maturation and structure-guided multimerization, we

105 optimized these agents and generated Spike binders that match or exceed the potency of most

106   monoclonal antibodies disclosed to date. Our lead neutralizing molecule, mNb6-tri, blocks

107   SARS-CoV-2 entry in human cells at picomolar efficacy and withstands aerosolization,

108   lyophilization, and elevated temperatures. mNb6-tri provides a promising approach to deliver a

109   potent SARS-CoV-2 neutralizing molecule directly to the airways for prophylaxis or therapy.

110

111   **RESULTS**

112   **Synthetic nanobodies that disrupt Spike-ACE2 interaction**

113   To isolate nanobodies that neutralize SARS-CoV-2, we screened a yeast surface-displayed

114   library of $>2x10^9$ synthetic nanobody sequences. Our strategy was to screen for binders to the

115   full Spike protein ectodomain, in order to capture not only those nanobodies that would compete

116   by binding to the ACE2-binding site on the RBD directly but also those that might bind

117   elsewhere on Spike and block ACE2 interaction through indirect mechanisms. We used a

118   mutant form of SARS-CoV-2 Spike (Spike*,) as the antigen (*15*). Spike* lacks one of the two

119   activating proteolytic cleavage sites between the S_1 and S_2 domains and introduces two

120   mutations to stabilize the pre-fusion conformation. Spike* expressed in mammalian cells binds

121   ACE2 with a K_D = 44 nM (Supplementary Fig. 1), consistent with previous reports (*17*). Next, we

122   labeled Spike* with biotin or with fluorescent dyes and selected nanobody-displaying yeast over

123   multiple rounds, first by magnetic bead binding and then by fluorescence-activated cell sorting

124   (Fig. 1A).

125

126   Three rounds of selection yielded 21 unique nanobodies that bound Spike* and showed

127   decreased Spike* binding in the presence of ACE2. Closer inspection of their binding properties

128   revealed that these nanobodies fall into two distinct classes. One group (Class I) binds the RBD

129   and competes with ACE2 (Fig. 1B). A prototypical example of this class is nanobody Nb6, which

130   binds to Spike* and to RBD alone with a K_D of 210 nM and 41 nM, respectively (Fig. 1C; Table

131   1). Another group (Class II), exemplified by nanobody Nb3, binds to Spike* (K_D = 61 nM), but

132   displays no binding to RBD alone (Fig. 1C, Table 1). In the presence of excess ACE2, binding of

133   Nb6 and other Class I nanobodies is blocked entirely, whereas binding of Nb3 and other Class II

134   nanobodies is decreased only moderately (Fig. 1B). These results suggest that Class I

135   nanobodies target the RBD to block ACE2 binding, whereas Class II nanobodies target other

136   epitopes and decrease ACE2 interaction with Spike allosterically or through steric interference.

137   Indeed, surface plasmon resonance (SPR) experiments demonstrate that Class I and Class II

138   nanobodies can bind Spike* simultaneously (Fig. 1D).

139

140   Analysis of the kinetic rate constants for Class I nanobodies revealed a consistently greater

141   association rate constant (k_a) for nanobody binding to the isolated RBD than to full-length Spike*

142   (Table 1), which suggests that RBD accessibility influences the K_D. We next tested the efficacy

143   of our nanobodies, both Class I and Class II, to inhibit binding of fluorescently labeled Spike* to

144   ACE2-expressing HEK293 cells (Table 1, Fig. 1E). Class I nanobodies emerged with highly

145   variable activity in this assay with Nb6 and Nb11 as two of the most potent clones with IC_{50}

146   values of 370 and 540 nM, respectively (Table 1). For unexplained reasons, Class II nanobodies

147   showed little to no activity in this assay (Table 1, Fig. 1E).

148

149   Going forward, we prioritized two Class I nanobodies, Nb6 and Nb11, that combine potent

150   Spike* binding with relatively small differences in k_a between binding to Spike* or RBD. We

151   reasoned that the epitopes recognized by Nb6 and Nb11 would be more readily accessible in

152   the Spike protein on intact virions. For Class II nanobodies we prioritized Nb3 because of its

153   optimal stability and yield during purification.

154

155   **Nb6 and Nb11 target the RBD and directly compete with ACE2**

156   To define the binding sites of Nb6 and Nb11, we determined their cryogenic electron

157   microscopy (cryo-EM) structures bound to Spike* (Fig. 2A-B, Supplementary Fig. 2-4,

158   Supplementary Table 1). Both nanobodies recognize RBD epitopes that overlap the ACE2

159   binding site (Fig. 2E). For Nb6 and Nb11, we resolved nanobody binding to both the open and

160   closed conformations of Spike*. We obtained a 3.0 Å map of Nb6 bound to closed Spike*, which

161   enabled modeling of the Nb6-Spike* complex (Fig. 2A), including the complementarity

162   determining regions (CDRs). We also obtained lower resolution maps for Nb6 bound to open

163   Spike* (3.8 Å), Nb11 bound to open Spike* (4.2 Å), and Nb11 bound to closed Spike* (3.7 Å).

164   For these lower resolution maps, we could define the nanobody's binding orientation but not

165   accurately model the CDRs.

166

167   Nb6 bound to closed Spike* straddles the interface between two adjacent RBDs. The majority of

168   the contacting surfaces are contributed by CDR1 and CDR2 of Nb6 (Fig. 2C). CDR3 contacts

169   the adjacent RBD that is counterclockwise positioned when viewed from the top of Spike* (Fig.

170   2C). The binding of one Nb6 therefore stabilizes two adjacent RBDs in the down-state. We

171   surmise that this initial binding event pre-organizes the binding site for a second and third Nb6

172   molecule to stabilize the closed Spike* conformation. Indeed, binding of two Nb6 molecules

173   would lock all three RBDs into the down-state, thus highly favoring binding of a third Nb6

5

174   because binding would not entail any further entropic cost. By contrast, Nb11 bound to down-

175   state RBDs only contacts a single RBD (Fig. 2D).

176

177   **Nb3 interacts with the Spike S$_1$ domain external to the RBD**

178   Our attempts to determine the binding site of Nb3 by cryo-EM proved unsuccessful. We

179   therefore turned to radiolytic hydroxyl radical footprinting to determine potential binding sites for

180   Nb3. Spike*, either apo or bound to Nb3, was exposed to 5-50 milliseconds of synchrotron X-ray

181   radiation to label solvent-exposed amino acids with hydroxyl radicals. Radical-labeled amino

182   acids were subsequently identified and quantified by mass spectrometry of trypsin/Lys-C or Glu-

183   C protease digested Spike*(18). Two neighboring surface residues on the S$_1$ domain of Spike

184   (M177 and H207) emerged as highly protected sites in the presence of Nb3 (Supplementary

185   Fig. 5). The degree of protection is consistent with prior observations of antibody-antigen

186   interactions by hydroxyl radical footprinting (19). Both M177 and H207 are greater than 40 Å

187   distant from the ACE2 binding site on the RBD, suggesting that Nb3 may inhibit Spike-ACE2

188   interactions through allosteric means.

189

190   **Rationally engineered multivalency increases potency**

191   The structure of Nb6 bound to closed Spike* enabled us to engineer bivalent and trivalent

192   nanobodies predicted to lock all RBDs in the down-state. To this end, we inserted flexible Gly-

193   Ser linkers of either 15 or 20 amino acids to span the 52 Å distance between adjacent Nb6

194   monomers bound to down-state RBDs in closed Spike* (Supplementary Fig. 6). Both linker

195   lengths are too short to span the distance (72 Å) between Nb6 bound to a down-state RBD and

196   an up-state RBD that would co-exist in an open Spike. Moreover, binding of three RBDs in the

197   previously reported conformation of Nb6-bound open Spike* would be physically impossible

198   even with longer linker length because of steric clashes (Supplementary Fig. 6). By contrast, the

199   minimum distance between adjacent Nb11 monomers bound to either open or closed Spike* is

200   68 Å (Supplementary Fig. 6). We therefore predicted that multivalent binding by Nb6 constructs

201   would display significantly slowed dissociation rates due to the enhanced avidity afforded by

202   Spike's trimeric architecture.

203

204   We assessed multivalent Nb6 binding to Spike* by SPR. Both bivalent Nb6 with a 15 amino acid

205   linker (Nb6-bi) and trivalent Nb6 with two 20 amino acid linkers (Nb6-tri) dissociate from Spike*

206   in a biphasic manner. The dissociation phase can be fitted to two components: a fast phase with

207   kinetic rate constants k_{d1} of 2.7×10^{-2} s^{-1} for Nb6-bi and 2.9×10^{-2} s^{-1} for Nb6-tri, which are of the

6

208   same magnitude as that observed for monovalent Nb6 ($k_d = 5.6 \times 10^{-2}$ s^{-1}) and a slow phase that

209   is dependent on avidity ($k_{d2} = 3.1 \times 10^{-4}$ for Nb6-bi and $k_{d2} < 1.0 \times 10^{-6}$ s^{-1} for Nb6-tri, respectively)

210   (Fig. 3A). The relatively similar k_d for the fast phase suggests that a fraction of the observed

211   binding for the multivalent constructs is nanobody binding to a single Spike* RBD. By contrast,

212   the slow dissociation phase of Nb6-bi and Nb6-tri indicates engagement of two or three RBDs.

213   We observed no dissociation for the slow phase of Nb6-tri over 10 minutes, indicating an upper

214   boundary for k_{d2} of 1×10^{-6} s^{-1} and subpicomolar affinity. This measurement remains an upper-

215   bound estimate rather than an accurate measurement because the technique is limited by the

216   intrinsic dissociation rate of Spike* from the chip imposed by the chemistry used to immobilize

217   Spike*.

218

219   We reasoned that the biphasic dissociation behavior could be explained by a slow

220   interconversion between up- and down-state RBDs, with conversion to the more stable down-

221   state required for full trivalent binding. According to this view, a single domain of Nb6-tri

222   engaged with an up-state RBD would dissociate rapidly. The system would then re-equilibrate

223   as the RBD flips into the down-state, eventually allowing Nb6-tri to trap all RBDs in closed

224   Spike*. To test this notion directly, we varied the time allowed for Nb6-tri binding to Spike*.

225   Indeed, we observed an exponential decrease in the percent fast-phase with a $t_{1/2}$ of 65 s (Fig.

226   3B), which, we surmise, reflects the timescale of conversion between the RBD up- and down-

227   states in Spike*. Taken together, dimerization and trimerization of Nb6 afforded 750-fold and

228   >200,000-fold gains in K_D, respectively.

229

230   **Class I and II nanobodies prevent SARS-CoV-2 infection**

231   We next tested the neutralization activity of trivalent versions of our top Class I (Nb6 and Nb11)

232   and Class II (Nb3) nanobodies against SARS-CoV-2 pseudotyped lentivirus. In this assay,

233   SARS-CoV-2 Spike is expressed as a surface protein on a lentiviral particle that contains a

234   ZsGreen reporter gene, which is integrated and expressed upon successful viral entry into cells

235   harboring the ACE2 receptor (20). Nb6 and Nb11 inhibited pseudovirus infection with IC$_{50}$

236   values of 2.0 µM and 2.4 µM, respectively, and Nb3 inhibited pseudovirus infection with an IC$_{50}$

237   of 3.9 µM (Fig. 3C, Table 1). Nb6-tri shows a 2000-fold enhancement of inhibitory activity, with

238   an IC$_{50}$ of 1.2 nM, whereas trimerization of Nb11 and Nb3 resulted in more modest gains of 40-

239   and 10-fold (51 nM and 400 nM), respectively (Fig. 3C).

240

241   We next confirmed these neutralization activities with a viral plaque assay using live SARS-

242   CoV-2 virus infection of VeroE6 cells. Consistent with its activity against pseudotyped lentivirus,

243   Nb6-tri proved exceptionally potent, neutralizing SARS-CoV-2 with an average IC_{50} of 160 pM

244   (Fig. 3D). Nb3-tri neutralized SARS-CoV-2 with an average IC_{50} of 140 nM (Fig. 3D).

245

246   **Affinity maturation yields a femtomolar K_D Spike inhibitor**

247   We further optimized the potency of Nb6 by selecting high-affinity variants. To this end, we

248   prepared a new library, starting with the Nb6 coding sequence, in which we varied each amino

249   acid position of all three CDRs by saturation mutagenesis (Fig. 4A). After two rounds of

250   magnetic bead-based selection, we isolated a population of high-affinity clones. Sequencing

251   revealed two highly penetrant mutations: I27Y in CDR1 and P105Y in CDR3. We incorporated

252   these two mutations into Nb6 to generate matured Nb6 (mNb6), which binds with 500-fold

253   increased affinity to Spike* as measured by SPR (Fig. 4B). As a monomer, mNb6 inhibits both

254   pseudovirus and live SARS-CoV-2 infection with low nanomolar potency, a ~200-fold

255   improvement compared to Nb6 (Fig. 4I-J, Table 1).

256

257   A 2.9 Å cryo-EM structure of mNb6 bound to Spike* shows that, like the parent nanobody Nb6,

258   mNb6 binds to closed Spike (Fig. 4C, Supplementary Fig. 7). The higher resolution map allowed

259   us to build a model with high confidence and determine the effects of the I27Y and P105Y

260   substitutions. mNb6 induces a slight rearrangement of the down-state RBDs as compared to

261   both previously determined structures of apo-Spike* and Spike* bound to Nb6, inducing a 9°

262   rotation of the RBD away from the central three-fold symmetry axis (Fig. 4H) (*14, 15*). This

263   deviation likely arises from a different interaction between CDR3 and Spike*, which nudges the

264   RBDs into a new resting position. While the I27Y substitution optimizes local contacts between

265   CDR1 in its original binding site on the RBD, the P105Y substitution leads to a marked

266   rearrangement of CDR3 in mNb6 (Fig. 4F-G). This conformational change yields a different set

267   of contacts between mNb6 CDR3 and the adjacent RBD (Fig. 4D). Remarkably, an X-ray crystal

268   structure of mNb6 alone revealed dramatic conformational differences in CDR1 and CDR3

269   between free and Spike*-bound mNb6, suggestive of significant conformational heterogeneity

270   for the unbound nanobodies and induced-fit rearrangements upon binding to Spike* (Fig. 4E).

271

272   The binding orientation of mNb6 is similar to that of Nb6, supporting the notion that our

273   multivalent design would likewise enhance binding affinity. Unlike Nb6-tri, trivalent mNb6

274   (mNb6-tri) bound to Spike with no observable fast-phase dissociation and no measurable

275 dissociation over ten minutes, yielding an upper bound for the dissociation rate constant k_d of

276 1.0×10^{-6} s^{-1} ($t_{1/2}$ > 8 days) and a K_D of <1 pM (Fig. 4B). As above, more precise measurements

277 of the dissociation rate are precluded by the surface chemistry used to immobilize Spike*.

278

279 mNb6-tri displays further gains in potency in both pseudovirus and live SARS-CoV-2 infection

280 assays with IC$_{50}$ values of 120 pM (5.0 ng/mL) and 54 pM (2.3 ng/mL), respectively (Fig. 4H-I,

281 Table 1). Given the sub-picomolar affinity observed by SPR, it is likely that these viral

282 neutralization potencies reflect the lower limit of the assays. mNb6-tri is therefore an

283 exceptionally potent SARS-CoV-2 neutralizing antibody, among the most potent molecules

284 disclosed to date.

285

286 **Nb6, Nb6-tri, mNb6, and mNb6-tri are robust proteins**

287 One of the most attractive properties that distinguishes nanobodies from traditional monoclonal

288 antibodies is their extreme stability (21). We therefore tested Nb6, Nb6-tri, mNb6, and mNb6-tri

289 for stability regarding temperature, lyophilization, and aerosolization. Temperature denaturation

290 experiments using circular dichroism measurements to assess protein unfolding revealed

291 melting temperatures of 66.9, 62.0, 67.6, and 61.4 °C for Nb6, Nb6-tri, mNb6 and mNb6-tri,

292 respectively (Fig 5A). Aerosolization and prolonged heating of Nb6, mNb6, and mNb6-tri for 1

293 hour at 50°C induced no loss of activity (Fig 5B). Moreover, mNb6 and mNb6-tri were stable to

294 lyophilization and to aerosolization using a mesh nebulizer, showing no aggregation by size

295 exclusion chromatography and preserved high affinity binding to Spike* (Fig. 5C-D).

296

297 **DISCUSSION**

298 There is a pressing need for prophylactics and therapeutics against SARS-CoV-2 infection.

299 Most recent strategies to prevent SARS-CoV-2 entry into the host cell aim at blocking the

300 ACE2-RBD interaction. High-affinity monoclonal antibodies, many identified from convalescent

301 patients, are leading the way as potential therapeutics (22-29). While highly effective *in vitro*,

302 these agents are expensive to produce by mammalian cell expression and need to be

303 intravenously administered by healthcare professionals (30). Moreover, large doses are likely to

304 be required for prophylactic viral neutralization, as only a small fraction of systemically

305 circulating antibodies cross the epithelial cell layers that line the airways (31). By contrast, single

306 domain antibodies (nanobodies) provide significant advantages in terms of production and

307 deliverability. They can be inexpensively produced at scale in bacteria *(E. coli)* or yeast *(P.*

308   *pastoris)*. Furthermore, their inherent stability enables aerosolized delivery directly to the nasal

309   and lung epithelia by self-administered inhalation (*32*).

310

311   Monomeric mNb6 is among the most potent single domain antibodies neutralizing SARS-CoV-2

312   discovered to date. Multimerization of single domain antibodies has been shown to improve

313   target affinity by avidity (*32, 33*). In the case of Nb6 and mNb6, however, our design strategy

314   enabled a multimeric construct that simultaneously engages all three RBDs, yielding profound

315   gains in potency. Furthermore, because RBDs must be in the up-state to engage with ACE2,

316   conformational control of RBD accessibility can serve as an added neutralization mechanism.

317   Indeed, our Nb6-tri and mNb6-tri molecules were designed with this functionality in mind. Thus,

318   when mNb6-tri engages with Spike, it prevents ACE2 binding by both directly occluding the

319   binding site and by locking the RBDs into an inactive conformation. Although a multitude of

320   other monoclonal and single-domain antibodies against SARS-CoV-2 Spike have been

321   discovered to date, there are few if any molecules as potent and stable as mNb6-tri (*33-43*).

322   Resistance to aerosolization, in particular, offers unprecedented opportunity for patient-friendly

323   nasal and pulmonary administration.

324

325   Our discovery of Class II neutralizing nanobodies demonstrates the presence of previously

326   unexplored mechanisms of blocking Spike binding to ACE2. For one Class II nanobody, Nb3,

327   we identified a likely binding site in the Spike S_1 domain external to the RBDs. Previously

328   discovered neutralizing antibodies from convalescent patients bind an epitope in a similar region

329   of Spike (*24, 26, 27*). Binding of Nb3 to this epitope may allosterically stabilize RBDs in the

330   down-state, thereby decreasing ACE2 binding. Pairing of Class I and Class II nanobodies in a

331   prophylactic or therapeutic cocktail could thus be a highly advantageous strategy for both potent

332   neutralization and prevention of escape variants. The combined stability, potency, and diverse

333   epitope engagement of our anti-Spike nanobodies therefore provide a unique potential

334   prophylactic and therapeutic strategy to limit the continued toll of the COVID-19 pandemic.

335

REFERENCES AND NOTES:

1. T. G. Ksiazek *et al.*, A novel coronavirus associated with severe acute respiratory syndrome. *N Engl J Med* **348**, 1953-1966 (2003).

2. A. M. Zaki, S. van Boheemen, T. M. Bestebroer, A. D. Osterhaus, R. A. Fouchier, Isolation of a novel coronavirus from a man with pneumonia in Saudi Arabia. *N Engl J Med* **367**, 1814-1820 (2012).

3. P. Zhou *et al.*, A pneumonia outbreak associated with a new coronavirus of probable bat origin. *Nature* **579**, 270-273 (2020).

4. J. F. Chan *et al.*, A familial cluster of pneumonia associated with the 2019 novel coronavirus indicating person-to-person transmission: a study of a family cluster. *Lancet* **395**, 514-523 (2020).

5. C. Huang *et al.*, Clinical features of patients infected with 2019 novel coronavirus in Wuhan, China. *Lancet* **395**, 497-506 (2020).

6. F. Wu *et al.*, A new coronavirus associated with human respiratory disease in China. *Nature* **579**, 265-269 (2020).

7. N. Zhu *et al.*, A Novel Coronavirus from Patients with Pneumonia in China, 2019. *N Engl J Med* **382**, 727-733 (2020).

8. World Health Organization. (2020).

9. Z. Ke *et al.*, Structures, conformations and distributions of SARS-CoV-2 spike protein trimers on intact virions. *bioRxiv*, 2020.2006.2027.174979 (2020).

10. B. J. Bosch, R. van der Zee, C. A. M. de Haan, P. J. M. Rottier, The coronavirus spike protein is a class I virus fusion protein: structural and functional characterization of the fusion core complex. *J. Virol.* **77**, 8801-8811 (2003).

11. Y. Cai *et al.*, Distinct conformational states of SARS-CoV-2 spike protein. *Science*, (2020).

12. Q. Wang *et al.*, Structural and Functional Basis of SARS-CoV-2 Entry by Using Human ACE2. *Cell* **181**, 894-904.e899 (2020).

13. R. Yan *et al.*, Structural basis for the recognition of SARS-CoV-2 by full-length human ACE2. *Science* **367**, 1444-1448 (2020).

14. A. C. Walls *et al.*, Structure, Function, and Antigenicity of the SARS-CoV-2 Spike Glycoprotein. *Cell* **181**, 281-292.e286 (2020).

15. D. Wrapp *et al.*, Cryo-EM structure of the 2019-nCoV spike in the prefusion conformation. *Science* **367**, 1260-1263 (2020).

16. M. Hoffmann *et al.*, SARS-CoV-2 Cell Entry Depends on ACE2 and TMPRSS2 and Is Blocked by a Clinically Proven Protease Inhibitor. *Cell* **181**, 271-280.e278 (2020).

17. J. Shang *et al.*, Structural basis of receptor recognition by SARS-CoV-2. *Nature* **581**, 221-224 (2020).

18. S. Gupta, J. Feng, L. J. Chan, C. J. Petzold, C. Y. Ralston, Synchrotron X-ray footprinting as a method to visualize water in proteins. *J Synchrotron Radiat* **23**, 1056-1069 (2016).

19. Y. Zhang, A. T. Wecksler, P. Molina, G. Deperalta, M. L. Gross, Mapping the Binding Interface of VEGF and a Monoclonal Antibody Fab-1 Fragment with Fast Photochemical Oxidation of Proteins (FPOP) and Mass Spectrometry. *J Am Soc Mass Spectrom* **28**, 850-858 (2017).

20. K. H. D. Crawford *et al.*, Protocol and Reagents for Pseudotyping Lentiviral Particles with SARS-CoV-2 Spike Protein for Neutralization Assays. *Viruses* **12**, (2020).

21. P. Kunz *et al.*, The structural basis of nanobody unfolding reversibility and thermoresistance. *Sci Rep* **8**, 7934 (2018).

22. A. Baum *et al.*, Antibody cocktail to SARS-CoV-2 spike protein prevents rapid mutational escape seen with individual antibodies. *Science*, (2020).

386 23. Y. Cao *et al.*, Potent Neutralizing Antibodies against SARS-CoV-2 Identified by High-
387   Throughput Single-Cell Sequencing of Convalescent Patients' B Cells. *Cell* **182**, 73-
388   84.e16 (2020).
389 24. X. Chi *et al.*, A neutralizing human antibody binds to the N-terminal domain of the Spike
390   protein of SARS-CoV-2. *Science*, (2020).
391 25. B. Ju *et al.*, Human neutralizing antibodies elicited by SARS-CoV-2 infection. *Nature*,
392   (2020).
393 26. L. Liu *et al.*, Potent neutralizing antibodies directed to multiple epitopes on SARS-CoV-2
394   spike. *Nature*, (2020).
395 27. D. Pinto *et al.*, Cross-neutralization of SARS-CoV-2 by a human monoclonal SARS-CoV
396   antibody. *Nature* **583**, 290-295 (2020).
397 28. T. F. Rogers *et al.*, Isolation of potent SARS-CoV-2 neutralizing antibodies and
398   protection from disease in a small animal model. *Science*, (2020).
399 29. S. J. Zost *et al.*, Potently neutralizing and protective human antibodies against SARS-
400   CoV-2. *Nature*, (2020).
401 30. H. Ledford, Antibody therapies could be a bridge to a coronavirus vaccine - but will the
402   world benefit? *Nature*, (2020).
403 31. V. H. Leyva-Grado, G. S. Tan, P. E. Leon, M. Yondola, P. Palese, Direct administration
404   in the respiratory tract improves efficacy of broadly neutralizing anti-influenza virus
405   monoclonal antibodies. *Antimicrob Agents Chemother* **59**, 4162-4172 (2015).
406 32. L. Detalle *et al.*, Generation and Characterization of ALX-0171, a Potent Novel
407   Therapeutic Nanobody for the Treatment of Respiratory Syncytial Virus Infection.
408   *Antimicrob Agents Chemother* **60**, 6-13 (2016).
409 33. D. Wrapp *et al.*, Structural Basis for Potent Neutralization of Betacoronaviruses by
410   Single-Domain Camelid Antibodies. *Cell* **181**, 1004-1015.e1015 (2020).
411 34. J. Huo *et al.*, Neutralizing nanobodies bind SARS-CoV-2 spike RBD and block
412   interaction with ACE2. *Nat. Struct. Mol. Biol.*, (2020).
413 35. J. D. Walter *et al.*, Sybodies targeting the SARS-CoV-2 receptor-binding domain.
414   *bioRxiv*, (2020).
415 36. Z. Sun *et al.*, Potent neutralization of SARS-CoV-2 by human antibody heavy-chain
416   variable domains isolated from a large library with a new stable scaffold. *MAbs* **12**,
417   1778435 (2020).
418 37. Y. Wu *et al.*, Identification of Human Single-Domain Antibodies against SARS-CoV-2.
419   *Cell Host Microbe* **27**, 891-898.e895 (2020).
420 38. T. J. Esparza, D. L. Brody, High Affinity Nanobodies Block SARS-CoV-2 Spike Receptor
421   Binding Domain Interaction with Human Angiotensin Converting Enzyme. *bioRxiv*,
422   2020.2007.2024.219857 (2020).
423 39. L. Hanke *et al.*, An alpaca nanobody neutralizes SARS-CoV-2 by blocking receptor
424   interaction. *bioRxiv*, 2020.2006.2002.130161 (2020).
425 40. T. F. Custódio *et al.*, Selection, biophysical and structural analysis of synthetic
426   nanobodies that effectively neutralize SARS-CoV-2. *bioRxiv*, 2020.2006.2023.165415
427   (2020).
428 41. T. Li *et al.*, Potent synthetic nanobodies against SARS-CoV-2 and molecular basis for
429   neutralization. *bioRxiv*, 2020.2006.2009.143438 (2020).
430 42. G. V. Nieto *et al.*, Fast isolation of sub-nanomolar affinity alpaca nanobody against the
431   Spike RBD of SARS-CoV-2 by combining bacterial display and a simple single-step
432   density gradient selection. *bioRxiv*, 2020.2006.2009.137935 (2020).
433 43. X. Chi *et al.*, Humanized Single Domain Antibodies Neutralize SARS-CoV-2 by
434   Targeting Spike Receptor Binding Domain. *bioRxiv*, 2020.2004.2014.042010 (2020).

44. D. Stadlbauer *et al.*, SARS-CoV-2 Seroconversion in Humans: A Detailed Protocol for a Serological Assay, Antigen Production, and Test Setup. *Curr. Protoc. Microbiol.* **57**, e100 (2020).

45. I. Lui *et al.*, Trimeric SARS-CoV-2 Spike interacts with dimeric ACE2 with limited intra-Spike avidity. *bioRxiv*, 2020.2005.2021.109157 (2020).

46. C. McMahon *et al.*, Yeast surface display platform for rapid discovery of conformationally selective nanobodies. *Nat. Struct. Mol. Biol.* **25**, 289-296 (2018).

47. D. N. Mastronarde, Automated electron microscope tomography using robust prediction of specimen movements. *J Struct Biol* **152**, 36-51 (2005).

48. S. Q. Zheng *et al.*, MotionCor2: anisotropic correction of beam-induced motion for improved cryo-electron microscopy. *Nat Methods* **14**, 331-332 (2017).

49. A. Punjani, J. L. Rubinstein, D. J. Fleet, M. A. Brubaker, cryoSPARC: algorithms for rapid unsupervised cryo-EM structure determination. *Nat Methods* **14**, 290-296 (2017).

50. J. Zivanov *et al.*, New tools for automated high-resolution cryo-EM structure determination in RELION-3. *Elife* **7**, (2018).

51. T. Grant, A. Rohou, N. Grigorieff, cisTEM, user-friendly software for single-particle image processing. *Elife* **7**, (2018).

52. J. Lan *et al.*, Structure of the SARS-CoV-2 spike receptor-binding domain bound to the ACE2 receptor. *Nature* **581**, 215-220 (2020).

53. S. G. Rasmussen *et al.*, Structure of a nanobody-stabilized active state of the β(2) adrenoceptor. *Nature* **469**, 175-180 (2011).

54. B. Frenz, A. C. Walls, E. H. Egelman, D. Veesler, F. DiMaio, RosettaES: a sampling strategy enabling automated interpretation of difficult cryo-EM maps. *Nat Methods* **14**, 797-800 (2017).

55. P. Emsley, K. Cowtan, Coot: model-building tools for molecular graphics. *Acta Crystallogr D Biol Crystallogr* **60**, 2126-2132 (2004).

56. T. I. Croll, ISOLDE: a physically realistic environment for model building into low-resolution electron-density maps. *Acta Crystallogr D Struct Biol* **74**, 519-530 (2018).

57. P. D. Adams *et al.*, PHENIX: a comprehensive Python-based system for macromolecular structure solution. *Acta Crystallogr D Biol Crystallogr* **66**, 213-221 (2010).

58. D. P. Staus *et al.*, Allosteric nanobodies reveal the dynamic range and diverse mechanisms of G-protein-coupled receptor activation. *Nature* **535**, 448-452 (2016).

59. S. Gupta, M. Sullivan, J. Toomey, J. Kiselar, M. R. Chance, The Beamline X28C of the Center for Synchrotron Biosciences: a national resource for biomolecular structure and dynamics experiments using synchrotron footprinting. *J Synchrotron Radiat* **14**, 233-243 (2007).

60. F. Yu *et al.*, Fast quantitative analysis of timsTOF PASEF data with MSFragger and IonQuant. *Mol Cell Proteomics*, (2020).

61. M. Choi *et al.*, MSstats: an R package for statistical analysis of quantitative mass spectrometry-based proteomic experiments. *Bioinformatics* **30**, 2524-2526 (2014).

62. W. Kabsch, Automatic processing of rotation diffraction data from crystals of initially unknown symmetry and cell constants. *Journal of Applied Crystallography* **26**, 795-800 (1993).

63. A. J. McCoy *et al.*, Phaser crystallographic software. *J Appl Crystallogr* **40**, 658-674 (2007).

64. B. E. Bricogne G., Brandl M., Flensburg C., Keller P., Paciorek W.,, S. A. Roversi P, Smart O.S., Vonrhein C., Womack T.O. , BUSTER version 1.10.0. . *Cambridge, United Kingdom: Global Phasing Ltd.*, (2017).

14

517   Pew Charitable Trusts, the Esther and A. & Joseph Klingenstein Fund and the Searle Scholars

518   Program.

519

Author Contributions

521   M.Schoof purified Spike*, RBD, and ACE2 proteins, performed yeast display selections to

522   identify and affinity mature nanobodies, expressed and purified nanobodies, tested activity in

523   cell-based assays, cloned, expressed, and purified multivalent nanobody constructs, and

524   coordinated live virus experiments. B.Faust purified and characterized Spike* protein and

525   candidate nanobodies, developed, performed and analyzed SPR experiments for Spike* and

526   RBD-nanobody affinity determination, developed, performed and analyzed SPR binning,

527   experiments, determined optimal freezing conditions for cryo-EM experiments, processed,

528   refined and generated figures for Nb6, Nb11, and mNb6 EM datasets. R.A. Saunders expressed

529   and purified ACE2 and nanobodies, developed and performed cell-based assays for inhibition of

530   Spike* binding and pseudovirus assays for determining nanobody efficacy. S.Sangwan

531   expressed and purified Spike*, RBD, ACE2-Fc, and nanobodies, processed cryo-EM data,

532   optimized RBD-nanobody complexes for crystallography, grew crystals of mNb6, collected

533   diffraction data, and refined the X-ray crystal structure of mNb6. V.Rezelj tested efficacy of

534   nanobody constructs in live SARS-CoV-2 infection assays under the guidance of M.Vignuzzi.

535   N.Hoppe purified nanobodies, developed, performed and analyzed SPR binning experiments,

536   developed performed and analyzed variable Nb6-bi and Nb6-tri association experiments, and

537   performed thermal melting stability assays for nanobody constructs. M.Boone developed

538   approaches to express and purify nanobodies from *Pichia pastoris* and developed, performed,

539   and analyzed approaches to quantify nanobody efficacy in live virus assays. C.B.Billesbølle

540   expressed and purified Spike*, generated affinity maturation library for Nb6, performed yeast

541   display selections to identify mNb6, and built the synthetic yeast nanobody library with J.Liang.

542   I.Deshpande expressed and purified nanobody constructs. B.S.Zha performed live SARS-CoV-2

543   virus assays to test nanobody efficacy with guidance from O.Rosenberg. C.R.Simoneau and

544   K.Leon performed live SARS-CoV-2 virus assays to test nanobody efficacy with guidance from

545   M.Ott. K.M.White performed live SARS-CoV-2 virus assays to test nanobody efficacy with

546   guidance from A.Garcia-Sastre. A.W.Barile-Hill performed SPR experiments. A.A.Anand,

547   N.Dobzinski, B.Barsi-Rhyne, and Y.Liu. assisted in cloning, expression, and purification of

548   nanobody and pseudovirus constructs. V.Belyy performed single-molecule nanobody-Spike*

549   interaction studies. S.Nock prepared media and coordinated lab usage during UCSF's partial

550   shutdown. M.Zimanyi and S.Gupta performed radiolytic footprinting experiments with guidance

15

551   from C.Y.Ralston and analyzed mass spectrometry data generated by D.L.Swaney. Several

552   members of the QCRG Structural Biology Consortium played an exceptionally important role for

553   this project. C.Azumaya and C.Puchades determined optimal freezing conditions for cryo-EM

554   experiments, optimized data collection approaches, and collected cryo-EM datasets. A.F.Brilot,

555   A.Rizo, A.M.Smith, F.Moss, D.Bulkley, T.Popsiech collected cryo-EM data on Spike*-nanobody

556   complexes. S.Dickinson, H.C.Nguyen, C.M.Chio, U.S.Chio, M.Gupta, M.Jin, F.Li, Y.Liu,

557   G.E.Merz, K.Zhang, M.Sun analyzed cryo-EM data from 15 Spike*-nanobody complex datasets.

558   H.T.Kratochvil set up crystallization trials of various RBD-nanobody complexes, and crystallized,

559   collected diffraction data for, and refined the mNb6 structure. M.C.Thompson collected,

560   processed, and refined the mNb6 structure. R.Trenker, D.Diwanji, K.Schaefer expressed and

561   purified Spike*, and S.Pourmal purified RBD. A.Manglik expressed and purified Spike*, labeled

562   Spike* for biochemical studies, designed selection strategies for nanobody discovery, cloned

563   nanobodies for expression, designed affinity maturation libraries and performed selections,

564   analyzed SPR data, and performed nanobody stability studies. The overall project was

565   supervised by P.Walter and A.Manglik.

566

567   **Competing Interests**

568   M.Schoof, B.Faust, R.A.Saunders, N.Hoppe, P.Walter, and A.Manglik are inventors on a

569   provisional patent describing anti-Spike nanobodies described in this manuscript.

570

571   **Data and Materials Availability**

572   All data generated or analyzed during this study are included in this published article and its

573   Supplementary Information. Crystallographic coordinates and structure factors for mNb6 have

574   been deposited in the Protein Data Bank under accession code XXXX. Coordinates for

575   Spike*:Nb6 and Spike*:mNb6 complexes have been deposited in the Protein Data Bank under

576   accession codes XXXX and XXXX, respectively. Maps for Spike*:Nb6, Spike*:Nb11, and

577   Spike*:mN6 have been deposited in the Electron Microscopy Data Bank under accession codes

578   XXXXX (Spike*-Nb6 Open), XXXXX (Spike*-Nb6 Closed), XXXXX (Spike*-Nb11 Open), XXXXX

579   (Spike*-Nb11 Closed), XXXXX (Spike*-mNb6 Closed). Plasmids for nanobody constructs used

580   in this study are available under a Material Transfer Agreement with the University of California,

581   San Francisco.

582

583   **MAIN TEXT FIGURES**

Figure 1
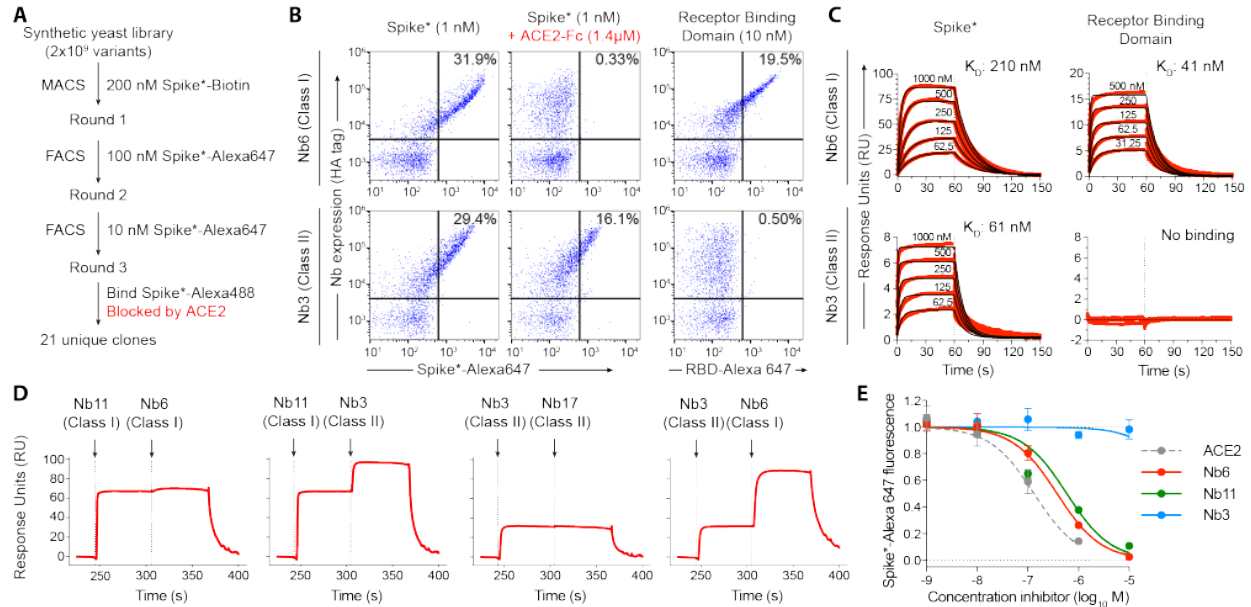
584

585

586   **Figure 1. Discovery of two distinct classes of anti-Spike nanobodies. A,** Selection strategy

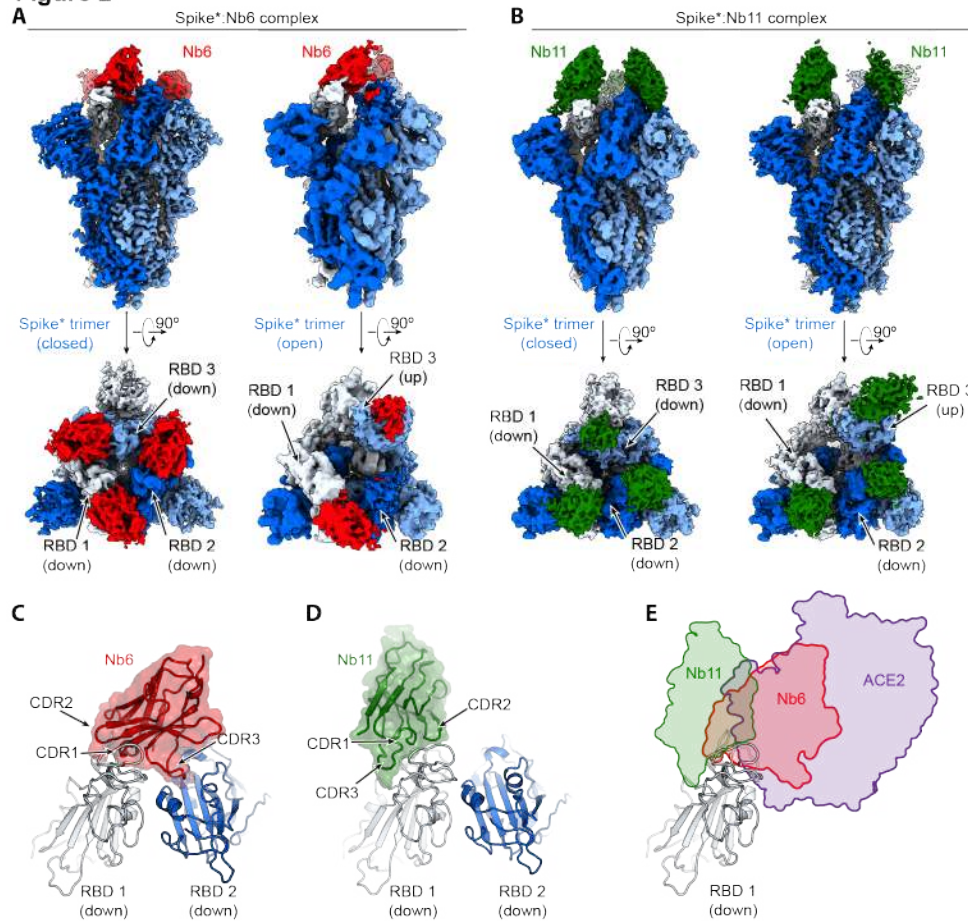587   for identification of anti-Spike nanobodies that disrupt Spike-ACE2 interactions using magnetic

588   bead selections (MACS) or fluorescence activated cell sorting (FACS). **B,** Flow cytometry of

589   yeast displaying Nb6 (a Class I nanobody) or Nb3 (a Class II nanobody). Nb6 binds Spike*-

590   Alexa 647 and receptor binding domain (RBD-Alexa 647). Nb6 binding to Spike* is completely

591   disrupted by an excess (1.4 μM) of ACE2-Fc. Nb3 binds Spike*, but not the RBD. Nb3 binding

592   to Spike* is partially decreased by ACE2-Fc. **C,** SPR of Nb6 and Nb3 binding to either Spike* or

593   RBD. Red traces are raw data and global kinetic fits are shown in black. Nb3 shows no binding

594   to RBD. **D,** SPR experiments with immobilized Spike* show that Class I and Class II nanobodies

595   can bind Spike* simultaneously. By contrast, two Class I nanobodies or Class II nanobodies do

596   not bind simultaneously. **E,** Nanobody inhibition of 1 nM Spike*-Alexa 647 binding to ACE2

597   expressing HEK293T cells. n = 3 (ACE2, Nb3) or 5 (Nb6, Nb11) biological replicates. All error

598   bars represent s.e.m.

17

Figure 2. Cryo-EM structures of Nb6 and Nb11 bound to Spike. A, Cryo-EM maps of Spike*-Nb6 complex in either closed (left) or open (right) Spike* conformation. **B,** Cryo-EM maps of Spike*-Nb11 complex in either closed (left) or open (right) Spike* conformation. The top views show receptor binding domain (RBD) up- or down-states. **C,** Nb6 straddles the interface of two down-state RBDs, with CDR3 reaching over to an adjacent RBD. **D,** Nb11 binds a single RBD in the down-state (displayed) or similarly in the up-state. No cross-RBD contacts are made by Nb11 in either RBD up- or down-state. **E,** Comparison of RBD epitopes engaged by ACE2 (purple), Nb6 (red), or Nb11 (green). Both Nb11 and Nb6 directly compete with ACE2 binding.

18
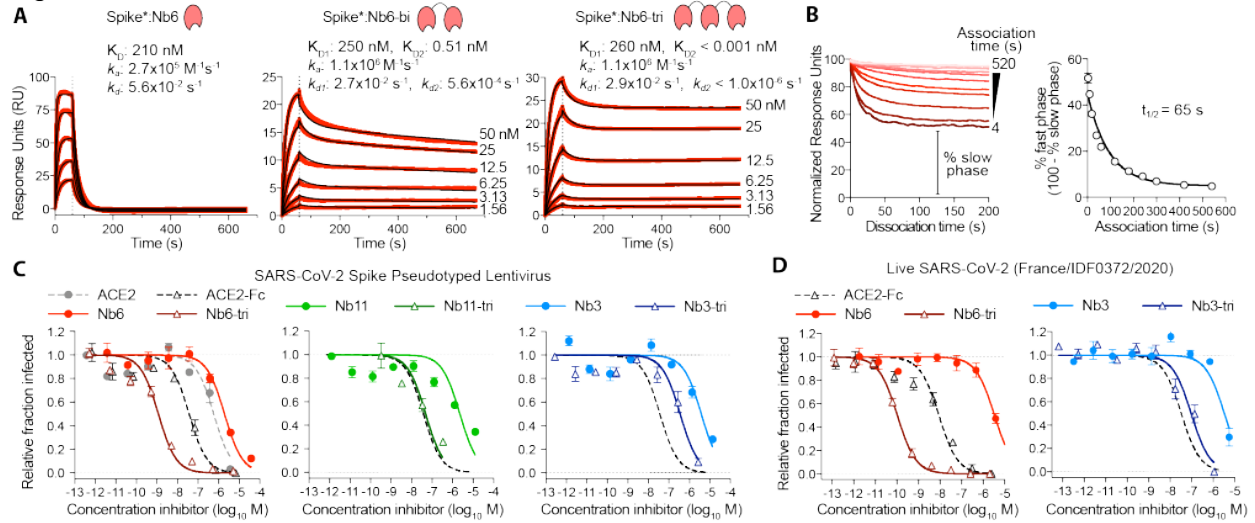
Figure 3. Multivalency improves nanobody affinity and inhibitory efficacy. A, SPR of Nb6 and multivalent variants. Red traces show raw data and black lines show global kinetic fit for Nb6 and independent fits for association and dissociation phases for Nb6-bi and Nb6-tri. **B,** Dissociation phase SPR traces for Nb6-tri after variable association time ranging from 4 to 520 s. Curves were normalized to maximal signal at the beginning of the dissociation phase. Percent fast phase is plotted as a function of association time (right) with a single exponential fit. n = 3 independent biological replicates. **C,** Inhibition of pseudotyped lentivirus infection of ACE2 expressing HEK293T cells. n = 3 biological replicates for all but Nb11-tri (n = 2) **D,** Inhibition of live SA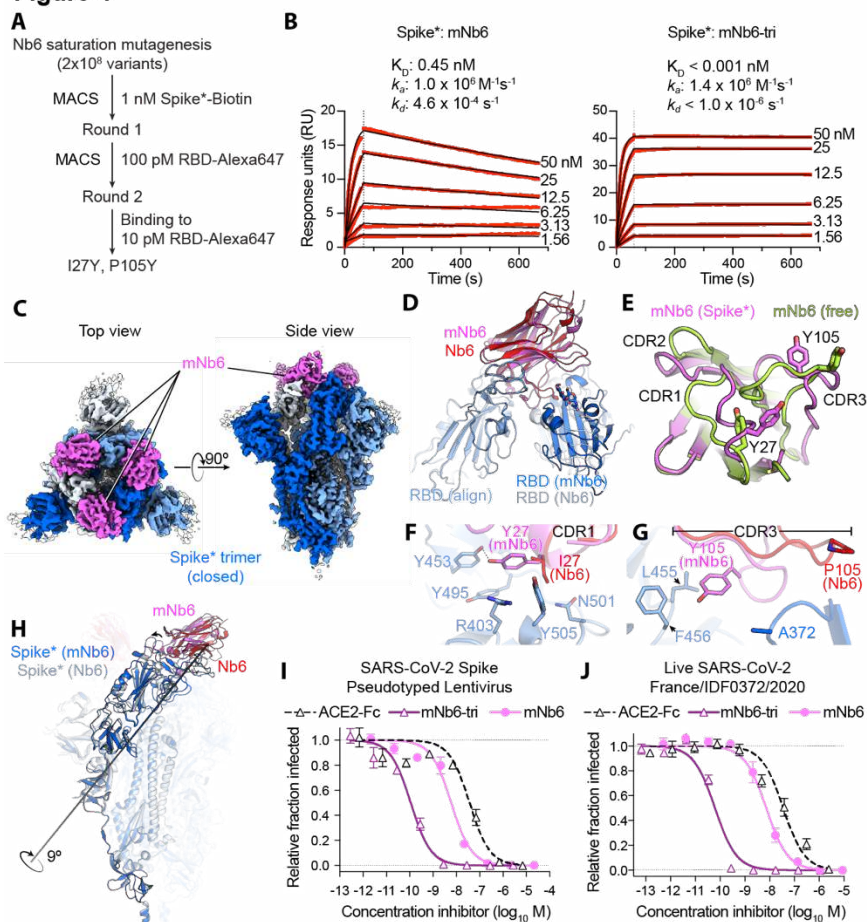RS-CoV-2 virus. Representative biological replicate with n = 3 (right panel) or 4 (left panel) technical replicates per concentration. n = 3 biological replicates for all but Nb3 and Nb3-tri (n = 2). All error bars represent s.e.m.

Figure 4. Affinity maturation of Nb6 yields a picomolar SARS-CoV-2 neutralizing molecule. A, A saturation mutagenesis library of Nb6 was subjected to two rounds of selection to identify consensus mutations I27Y and P105Y. **B,** SPR of mNb6 and mNb6-tri binding to immobilized Spike*. Red traces show raw data and black lines show global kinetic fit. No dissociation was observed for mNb6-tri over 10 minutes. **C,** Cryo-EM structure of Spike*-mNb6 complex. **D,** Comparison of receptor binding domain (RBD) engagement by Nb6 and mNb6. One RBD was used to align both structures (RBD align), demonstrating changes in Nb6 and mNb6 position and the adjacent RBD. **E,** Comparison of mNb6 complementarity determining regions in either the cryo-EM structure of the Spike*-mNb6 complex or an X-ray crystal structure of mNb6 alone. **F,** CDR1 of Nb6 and mNb6 binding to the RBD. As compared to I27 in Nb6, Y27 of mNb6 hydrogen bonds to Y453 and optimizes pi-pi and pi-cation interactions with the RBD. **G,** CDR3 of Nb6 and mNb6 binding to the RBD demonstrating a large conformational rearrangement of the entire loop in mNb6. **H,** Comparison of closed Spike* bound to mNb6 and Nb6. Rotational axis for RBD movement is highlighted. **I,** Inhibition of pseudotyped lentivirus infection of ACE2 expressing HEK293T cells by mNb6 and mNb6-tri. n = 3 biological replicates

20

639   **J,** mNb6 and mNb6-tri inhibit SARS-CoV-2 infection of VeroE6 cells in a plaque assay.

640   Representative biological replicate with n = 4 technical replicates per concentration. n = 3

641   biological replicates for all samples. All error bars represent s.e.m.

642
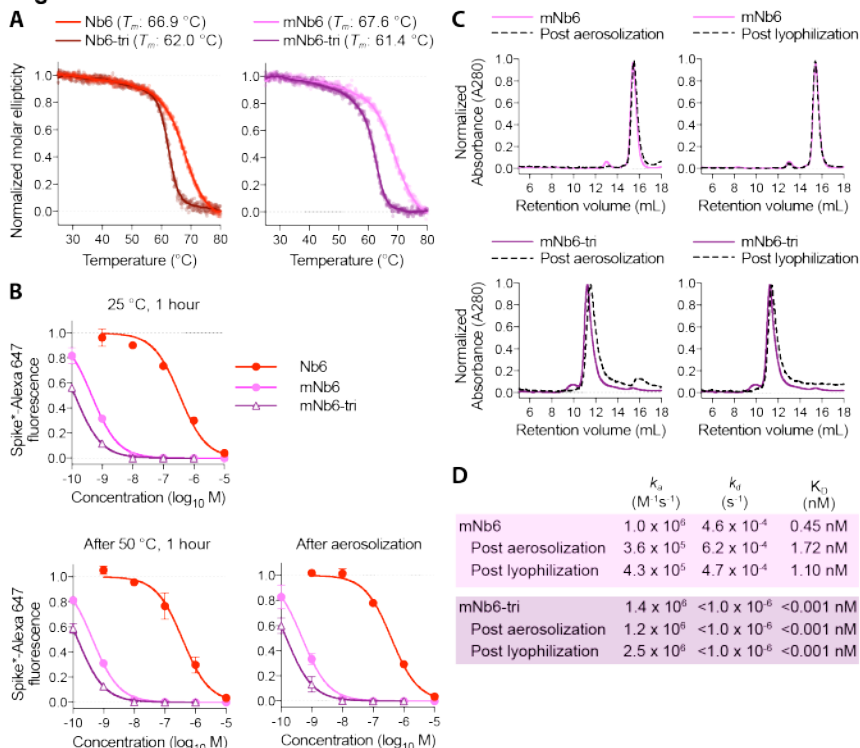
Figure 5. Nb6 and its derivates are robust proteins. A, Thermal denaturation of nanobodies assessed by circular dichroism measurement of molar ellipticity at 204 nm. Apparent melting temperatures (T_m) for each nanobody are indicated. **B,** Nanobody inhibition of 1 nM Spike*-Alexa 647 binding to ACE2 expressing HEK293T cells after incubation at either 25 °C or 50 °C for 1 hour or after aerosolization. **C,** Size exclusion chromatography of nanobodies after lyophilization or aerosolization. **D,** Summary table of SPR kinetics data and affinities for aerosolized or lyophilized mNb6 and mNb6-tri.

22

652 **Table 1. Anti-Spike nanobody affinity and neutralization potency**

Nanobody	Class	Spike* Binding k_a (M^{-1}s^{-1})	k_d (s^{-1})	K_D (M)	RBD Binding k_a (M^{-1}s^{-1})	k_d (s^{-1})	K_D (M)	Spike* Competition IC$_{50}$ (s.e.m) (M)[a]	SARS-CoV-2 Pseudovirus IC$_{50}$ (s.e.m.) (M)[b]	Live SARS-CoV-2 IC$_{50}$ (s.e.m.) (M)[c]
Nb2	I	9.0×10^5	5.3×10^{-1}	5.9×10^{-7}	1.0×10^6	9.9×10^{-1}	9.7×10^{-7}	8.3×10^{-6} (1.7×10^{-6})	NP	NP
Nb3	II	1.8×10^6	1.1×10^{-1}	6.1×10^{-8}	NB			NC	3.9×10^{-6} (7.9×10^{-7})	3.0×10^{-6} (3.2×10^{-7})
Nb6	I	2.7×10^5	5.6×10^{-2}	2.1×10^{-7}	2.1×10^6	8.7×10^{-2}	4.1×10^{-8}	3.7×10^{-7} (4.9×10^{-8})	2.0×10^{-6} (3.5×10^{-7})	3.3×10^{-6} (7.2×10^{-7})
Nb8	I	1.4×10^5	8.1×10^{-1}	5.8×10^{-6}	6.6×10^5	3.3×10^{-1}	5.1×10^{-7}	4.8×10^{-6} (4.9×10^{-7})	NP	NP
Nb11	I	1.2×10^6	1.6×10^{-1}	1.4×10^{-7}	3.2×10^6	2.4×10^{-1}	7.6×10^{-8}	5.4×10^{-7} (1.2×10^{-7})	2.4×10^{-6} (5.4×10^{-7})	NP
Nb12	I	1.2×10^2	2.0×10^{-4}	1.6×10^{-6}	Biphasic	Biphasic	Biphasic	2.5×10^{-7} (5.5×10^{-8})	1.2×10^{-6} (9.0×10^{-7})	NP
Nb15	I	1.7×10^5	2.3×10^{-1}	1.3×10^{-6}	6.0×10^5	2.2×10^{-1}	3.6×10^{-7}	2.2×10^{-6} (2.5×10^{-7})	6.7×10^{-6} (3.6×10^{-6})	NP
Nb16	I	1.1×10^5	1.3×10^{-1}	1.3×10^{-6}	NP			9.5×10^{-7} (1.1×10^{-7})	NP	NP
Nb17	II	7.3×10^5	2.0×10^{-1}	2.7×10^{-7}	NB			NC	7.6×10^{-6} (1.0×10^{-6})	NP
Nb18	II	1.4×10^5	6.4×10^{-3}	4.5×10^{-8}	NB			5.2×10^{-5} (1.5×10^{-5})	NP	NP
Nb19	I	2.4×10^4	1.1×10^{-1}	4.5×10^{-6}	1.0×10^5	8.9×10^{-2}	8.8×10^{-7}	4.1×10^{-6} (4.9×10^{-7})	2.4×10^{-5} (7.7×10^{-6})	NP
Nb24	I	9.3×10^5	2.7×10^{-1}	2.9×10^{-7}	2.4×10^6	3.5×10^{-1}	1.5×10^{-7}	7.5×10^{-7} (1.0×10^{-7})	NP	NP
ACE2	N/A	2.7×10^5	1.2×10^{-2}	4.4×10^{-8}	NP	NP	NP	1.7×10^{-7} (6.6×10^{-8})	6.2×10^{-7} (1.7×10^{-7})	NP
mNb6	I	1.0×10^6	4.5×10^{-4}	4.5×10^{-10}	1.1×10^6	6.4×10^{-4}	5.6×10^{-10}	1.3×10^{-9} (4.1×10^{-10})	6.3×10^{-9} (1.6×10^{-9})	1.2×10^{-8} (2.5×10^{-9})
Nb3-bi	II	NP	NP	NP	NP	NP	NP	NP	3.6×10^{-7} (1.5×10^{-7})	1.8×10^{-7} (1.2×10^{-8})
Nb3-tri	II	Biphasic	Biphasic	Biphasic	NP	NP	NP	4.1×10^{-8} (1.6×10^{-8})	4.0×10^{-7} (1.6×10^{-7})	1.4×10^{-7} (4.9×10^{-8})
Nb6-bi	I	Biphasic	Biphasic	Biphasic	NP	NP	NP	NP	6.3×10^{-8} (1.5×10^{-8})	NP
Nb6-tri	I	Biphasic	Biphasic	Biphasic	NP	NP	NP	1.5×10^{-9} (5.2×10^{-10})	1.2×10^{-9} (2.5×10^{-10})	1.6×10^{-10} (2.6×10^{-11})
Nb11-tri	I	Biphasic	Biphasic	Biphasic	NP	NP	NP	NP	5.1×10^{-8} (1.6×10^{-8})	NP
ACE2-Fc	N/A	NP	NP	NP	NP	NP	NP	5.3×10^{-9} (2.5×10^{-9})	4.0×10^{-8} (8.8×10^{-9})	2.6×10^{-8} (8.5×10^{-9})
mNb6-tri	I	1.4×10^6	$<1.0\times10^{-6}$	$<1.0\times10^{-12}$	NP	NP	NP	4.0×10^{-10} (1.4×10^{-10})	1.2×10^{-10} (2.8×10^{-11})	5.4×10^{-11} (1.0×10^{-11})

653

654 [a]Average values from n = 5 biological replicates for Nb6, Nb11, Nb15, Nb19 are presented, all

655 others were tested with n = 3 biological replicates.

23

656   [b]Average values from n = 2 biological replicates for Nb12, Nb17, and Nb11-tri are presented, all

657   others were tested with n = 3 biological replicates.

658   [c]Average values from n = 2 biological replicates for Nb3, Nb3-bi, and Nb3-tri. n = 3 biological

659   replicates for all others.

660   NB – no binding

661   NC – no competition

662   NP – not performed